




# Long-wavelength infrared selective emitter for thermal infrared camouflage under a hot environment

JINGUO ZHANG,<sup>1,2</sup> ZHENGJI WEN,<sup>2,7</sup>  ZIJI ZHOU,<sup>2</sup>  
DONGJIE ZHOU,<sup>2</sup> QIANLI QIU,<sup>2</sup> JUN GE,<sup>2</sup> YONGXING ZENG,<sup>3</sup>  
YAN SUN,<sup>2,8</sup> LEI ZHOU,<sup>4</sup> NING DAI,<sup>2,5</sup> JUNHAO CHU,<sup>2,6</sup>  
AND JIAMING HAO<sup>2,6,9</sup>

<sup>1</sup>School of Physical Science and Technology, ShanghaiTech University, Shanghai 201210, China

<sup>2</sup>State Key Laboratory of Infrared Physics, Shanghai Institute of Technical Physics, Chinese Academy of Science, Shanghai 200083, China

<sup>3</sup>Unit 32215 of PLA, Beijing 100093, China

<sup>4</sup>State Key Laboratory of Surface Physics and Key Laboratory of Micro and Nano Photonic Structures (Ministry of Education), and Physics Department, Fudan University, Shanghai 200433, China

<sup>5</sup>Hangzhou Institute for Advanced Study, University of Chinese Academy of Sciences, Hangzhou 310024, China

<sup>6</sup>Institute of Optoelectronics, Fudan University, Shanghai 200433, China

<sup>7</sup>wenzhengji@mail.sitp.ac.cn

<sup>8</sup>sunny@mail.sitp.ac.cn

<sup>9</sup>jmhao@fudan.edu.cn

**Abstract:** Thermal infrared camouflage as a kind of counter-surveillance technique has attracted much attention owing to the rapid development of infrared surveillance technology. Various artificial optical structures have been developed for infrared camouflage applications under cold ambient environment (low thermal radiation), but the realization of infrared camouflage under a hot environment (high thermal radiation) is also highly desirable and has been rarely reported. Here, a lithography-free, ultra-thin, high performance long-wavelength infrared (LWIR) selective emitter for thermal infrared camouflage in a high radiation environment is proposed and experimentally demonstrated. Experimental results show that our designed selective emitter exhibits average emissivity higher than 90% over the LWIR range from 8 to 14  $\mu\text{m}$  and low emissivity less than 35% outside this window. Numerical simulations were performed to optimize the geometrical structures and reveal that such a selective emission effect is attributed to the combination of multiple hybrid plasmonic resonances. LWIR thermal images show that the selective emitter can perfectly blend into the high radiation backgrounds. Furthermore, it is found that the sample displays angle-independent emission properties, indicating that our emitter offers great potential for application in evading large-angle detection.

© 2022 Optica Publishing Group under the terms of the [Optica Open Access Publishing Agreement](#)

## 1. Introduction

Long-wavelength infrared (LWIR) ranging from 8 to 14  $\mu\text{m}$  is one of the most important atmospheric transparent windows where the electromagnetic radiation emitted by terrestrial temperature objects mostly lies in this spectral region, as it is also regarded as “thermal infrared” [1–9]. Although the wavelength is far beyond the range of what human eyes can see, infrared cameras operating in this range can detect the radiation and recognize the objects. As the rapid development of infrared surveillance technology, infrared camouflage, as a kind of counter-surveillance techniques, has drawn much attention recently [10–13]. The so-called thermal infrared camouflage is to control the thermal radiation of given objects for matching the

surroundings, so that the targets can blend into the ambient environment, and thus be “invisible” to thermal infrared equipment. According to the Stefan-Boltzmann law ( $Q = \epsilon\sigma T^4$ ,  $\sigma$  is the Stefan-Boltzmann constant), the radiation power  $Q$  of an object is strongly dependent on the emissivity  $\epsilon$  and the Kelvin temperature  $T$ . It is thus that manipulating the emissivity is of practical significance for thermal infrared camouflage, particularly for objects that have the same temperature with the ambient environment [14]. Over the past years, based on this strategy, various artificial optical structures, such as, photonic crystals [15,16], metamaterials [17–20], metasurfaces [21–26], 2D materials [27,28] and layered materials [29,30] have been widely investigated for infrared camouflage applications. However, although remarkable camouflage performances have been achieved by using such artificial structures, their applications are practically restricted by the complicated preparation process and high cost; more notably, most of studies were focused on the design of wavelength-selective emitters for concealing the objects at the “cold” ambient environment that has weak thermal radiation (low emissivity) in the LWIR atmospheric transparent window [31–40], but it is rarely reported for the “hot” environment with high thermal radiation (high emissivity) in previous literatures, which is also very important for some specific application scenarios, such as hiding vehicles in hot desert from infrared detection.

In this work, we present a lithography-free, ultra-thin, high performance LWIR selective emitter for thermal infrared camouflage at high radiation environment. The configuration of our design is comprised of four-layer metal-hemispheres-semiconductor-metal thin film. The second layer is a monolayer of polystyrene (PS) micro-hemisphere array prepared by means of a simple self-assembly technique [41–44], which enables our designed emitter to be fabricated in a large area at low cost compared with traditional optical structures [45]. The fabricated selective emitter exhibits average emissivity higher than 90% over the range from 8 to 14  $\mu\text{m}$ , meanwhile, maintains low emissivity less than 35% outside this window. Suppressing radiation outside the atmospheric window would be beneficial for the emitter to reduce heat dissipation and keep high thermal radiation characteristic over the LWIR region, yielding superior thermal camouflage performance under hot environment. Numerical simulations were carried out to optimize the geometrical structures and reveal that such selective emission effect is attributed to the combination of multiple hybrid plasmonic resonances. LWIR images show that the sample can really be hidden in the high radiation background. Furthermore, it is found that the sample displays angle-independent emission properties, indicating that our emitter possesses the capability for large-angle thermal infrared camouflage.

## 2. Results and discussion

The fabrication process of the LWIR selective emitter is illustrated in Fig. 1. Firstly, self-assembly technique was used to produce homogeneous, close-packed polystyrene (PS) microspheres template on a thick gold film (Fig. 1(a)). Then, oxygen plasma reactive ion etching (RIE) was used to etch the shape of PS microspheres (Fig. 1(b)). Scanning electron microscopy (SEM) images of a fabricated sample at these two preparation stages are shown in Fig. 7. After that, rapid thermal annealing process was conducted to form PS hemisphere arrays under the action of surface tension (Au-PS hemispheres, labeled as AP), as shown in Fig. 1(c).

Figure 2(a-c) shows an enlarged schematic diagram of the AP structure and cross-section view and top view SEM images of a sample after the process of rapid thermal annealing, respectively. Determined from the (SEM) images, a highly ordered PS hemispherical array structure (the distance between the centers of the two neighboring PS hemispheres  $p = 1.8 \mu\text{m}$ ) was obtained. Since PS hemispheres are transparent within the region of interest (5–15  $\mu\text{m}$ ), the infrared light can directly reach the bottom Au film which is highly reflective, hence, this stage exhibits high reflection and low emission, as observed from the experimental spectra shown in Fig. 2(d). By virtue of Kirchoff’s law of thermal radiation, the spectral-directional emissivity of an object is the same as its corresponding absorptance under thermal equilibrium. The emissivity ( $E$ ) is thus

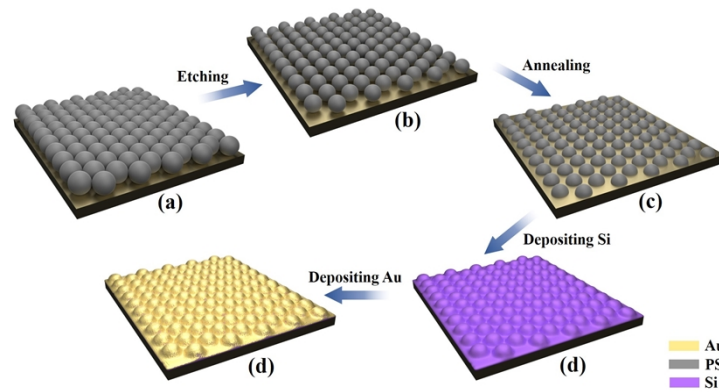


**Fig. 1.** Schematic illustration of the fabrication process of the LWIR selective emitter. (a) A monolayer of polystyrene (PS) microsphere array self-assembled on a gold film. (b) Etching the shape of microspheres by oxygen plasma RIE. (c) Thermal annealing at 210 °C for 15 min to construct hemispherical arrays. (d) Depositing 500 nm Si film on PS hemispherical array. (e) LWIR selective emitter obtained after depositing a thin layer of Au film.

obtained by  $E = A = 1 - R$ , here  $A$  and  $R$  denote the absorptance and reflectance of the structure, respectively.

Next step, a layer of amorphous Si (~500 nm) was deposited on top of the PS hemispheres to form an Au-PS hemispheres-Si (labeled as APS) structure, as illustrated in Fig. 1(d) (An enlarged schematic diagram of the APS structure is also shown in Fig. 2(e)). The corresponding cross-section view and top view SEM images of a fabricated APS sample are shown in Fig. 2(f, g). The measured reflectance and emissivity spectra of the structure are presented in Fig. 2(h), which exhibit emissivity over 40% within the wavelength range 9.7-11.5  $\mu\text{m}$ . Compared to AP structure, noticeable enhancement of LWIR radiation of the APS structure has been achieved, however, no matter the bandwidth or efficiency of the structure are still needed to be increased for the application of thermal camouflage in high thermal radiation environment.

To enhance the emissivity, a thin Au film was further introduced to cover on the top of Si-coated PS hemispheres and build an Au-hemispheres-Si-Au (APSA) structure, as illustrated in Fig. 1(e) and Fig. 2(i). In order to acquire an optimized device that can be useful to disguise in high LWIR radiation background, experiments were carried out to investigate how the geometric parameters influence the optical properties of the structure. Figure 3(a) shows the measured emissivity as a function of the thickness ( $t$ ) of the top gold film, with the other parameters taken as  $p = 1.8 \mu\text{m}$ ,  $r = 0.6 \mu\text{m}$  and  $h = 0.5 \mu\text{m}$ , where  $r$  and  $h$  denote the radius of polymeric hemispheres and the thickness of the Si film, respectively. It is found that as  $t$  increases, the average emissivity of the structure increases first until reaching the maximum due to the resonance enhancement, and then decreases over the LWIR range because of the reflection [46]. For clarity, the emissivity spectra for three typical thickness top gold films ( $t = 4, 7$  and  $10 \text{ nm}$ ) are replotted in Fig. 3(b). There really exists a critical thickness  $t = 7 \text{ nm}$  where the structure has the maximum average emissivity. Numerical simulations were performed to verify the experimental observations, the simulated results are shown correspondingly in Fig. 3(c) and Fig. 3(d). Good agreements are found between the measured and theoretical results.

The dependence of thermal emission properties on the other parameters (the radius  $r$  of polymeric hemispheres, the thickness  $h$ , optical constant of the middle spacer layer and material of bottom metal film) were also investigated and presented in Fig. 8. Figure 2(j-l) exhibit cross-section view, top-view SEM images and the measured reflectance and emissivity of a fabricated APSA sample with optimized parameters ( $p = 1.8 \mu\text{m}$ ,  $r = 0.6 \mu\text{m}$ ,  $h = 0.5 \mu\text{m}$  and

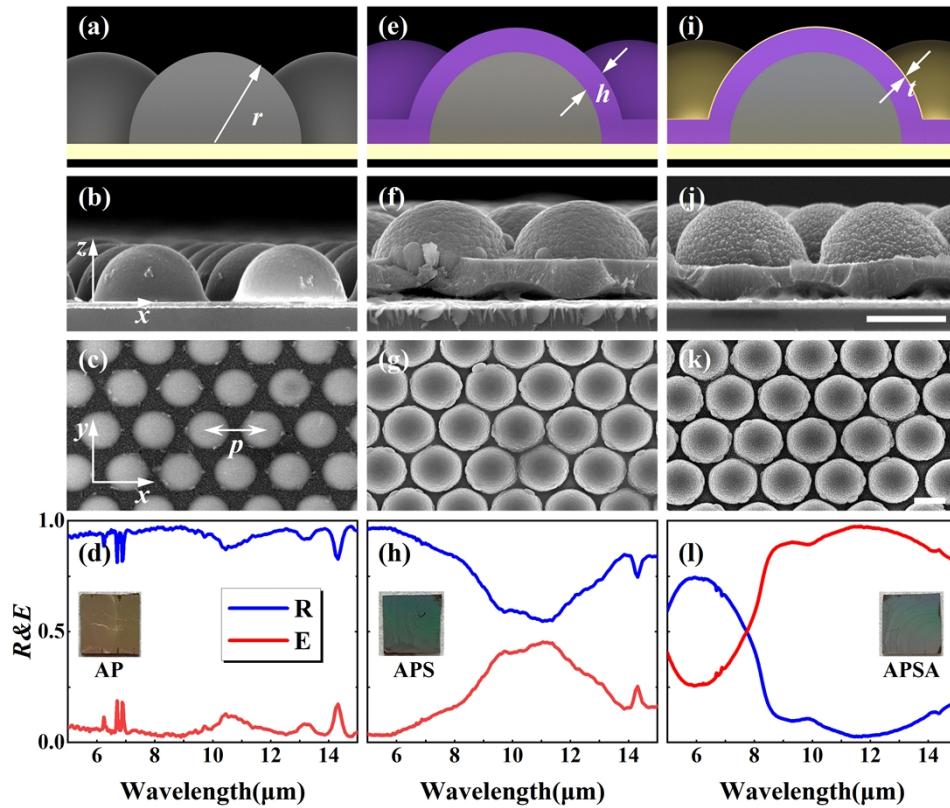


**Fig. 2.** Schematic diagrams of our proposed structure at different stages. (a) Au-polystyrene hemispheres (labeled AP).  $r$  denotes the radius of the PS hemispheres. (e) Au-polystyrene hemispheres-Si (labeled APS). (i) Au-polystyrene hemispheres-Si-Au (labeled APSA).  $h$  and  $t$  represent the thickness of Si and Au, respectively. (b, f, j) Cross-section view and (c, g, k) top-view SEM images of an experimental sample at each corresponding stages, scale bars: 1  $\mu\text{m}$ .  $p$  represents the distance between the centers of the two neighboring PS hemispheres. (d, h, l) Experimental measured reflectance ( $R$ ) and emissivity ( $E$ ) spectra at each stage. Insets are the photographs of the structure at different stages.

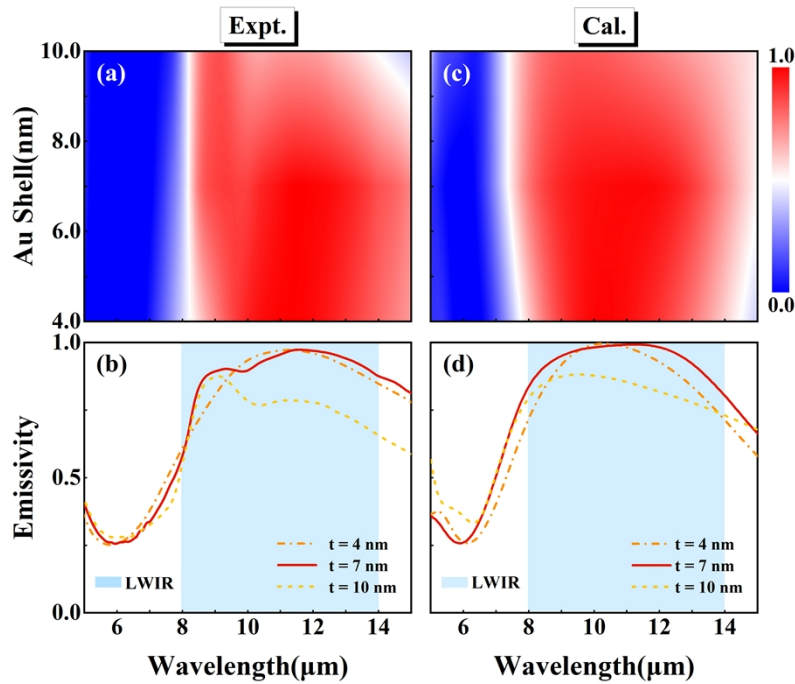


**Fig. 3.** (a) Measured and (c) simulated emissivity mapping spectra of the proposed APSA emitter versus wavelengths and the thickness of top Au layers. (b) Measured and (d) simulated emissivity spectra for three typical thickness of top Au layers ( $t = 4, 7,$  and  $10$  nm). Shaded area denotes the scope of LWIR spectral region.

$t = 7$  nm). It notes that the emitter exhibits average emissivity higher than 90% over the entire LWIR region (from  $8$  to  $14$   $\mu\text{m}$ ), and has low emissivity less than 35% in non-atmospheric window range from  $5$ - $8$   $\mu\text{m}$ , which is promising for its potential of thermal camouflage in high LWIR radiation background.

To understand the nature of our proposed device, we performed numerical simulations to investigate the electromagnetic field distributions. Figure 4 shows the magnitude of electric and magnetic fields for four different wavelengths  $8$   $\mu\text{m}$ ,  $10$   $\mu\text{m}$ ,  $10.7$   $\mu\text{m}$  and  $12$   $\mu\text{m}$ , respectively. In our simulation, the structure was excited by a normally incident plane wave with the electric field parallel to  $y$ -axis, and the field monitors were placed at  $z = 700$  nm. As can be observed, at the longer wavelength of  $12$   $\mu\text{m}$ , the electric field is mostly distributed around the surface of the top gold films, and the magnetic field is highly concentrated inside the hemispheres, it exhibits the same features as the fundamental localized resonant mode of conventional metal-insulator-metal (MIM) structure [47–50]. In contrast, at the shorter wavelengths  $8$   $\mu\text{m}$  and  $10$   $\mu\text{m}$ , both the electric and magnetic fields are strongly concentrated in the gaps between the gold covered hemispheres; the field profiles are similar to those of whispering gallery modes [51]. While, the field distributions at  $10.7$   $\mu\text{m}$  hold a combination of the two characteristics described above, which are not only localized around the surface of the gold films and inside the hemispheres, but also confined in certain domain between the nearby hemispheres. All these results indicate that the underlying mechanism of the broadband emission/absorption is originated from the joint effects of multiple hybrid plasmonic resonant modes (see more details in Fig. 9).

To demonstrate the performance of thermal infrared camouflage, experiments of the proposed selective emitter hidden in two different types of backgrounds were conducted. In the first case, the AP, APS and APSA samples were placed on the author's palm that is highly radiative over

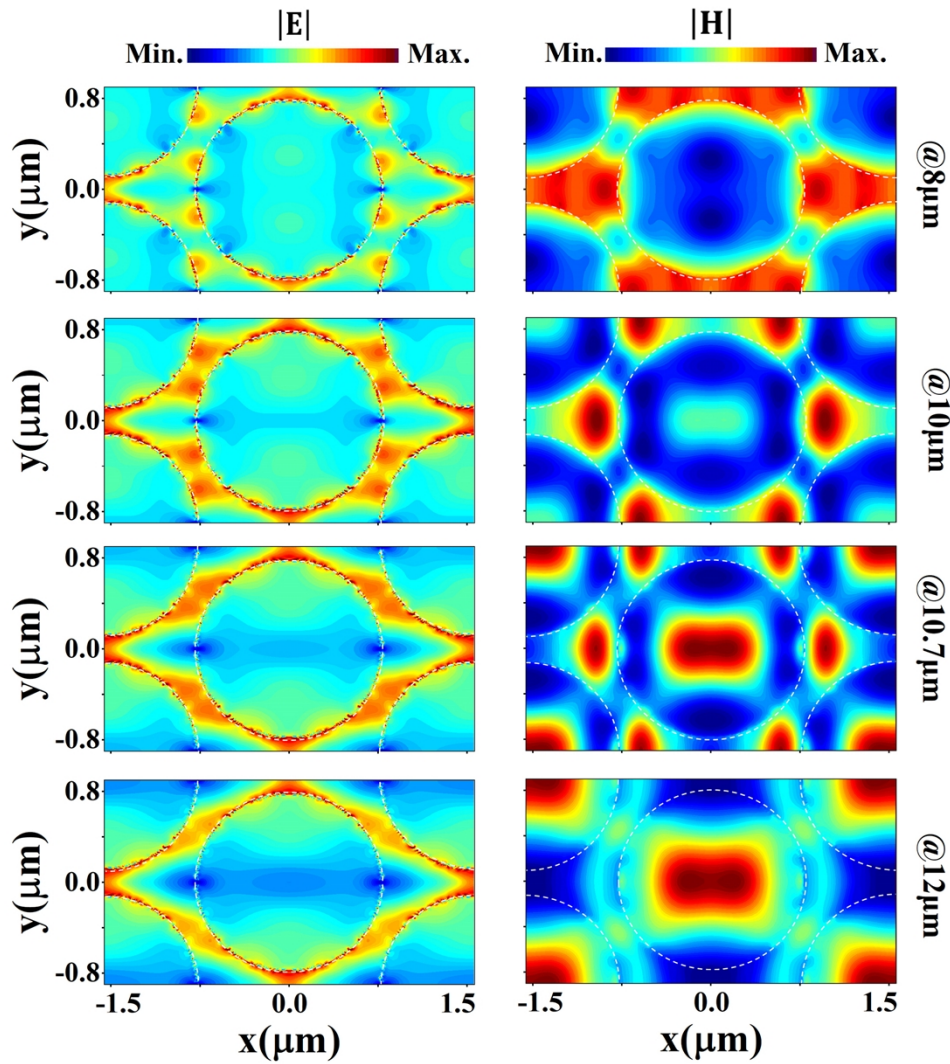


**Fig. 4.** Magnitude of electric fields  $|E|$  and magnetic fields  $|H|$  of the APSA structure in  $x$ - $y$  plane ( $z = 0.7 \mu\text{m}$ ) for four different wavelengths  $8 \mu\text{m}$ ,  $10 \mu\text{m}$ ,  $10.7 \mu\text{m}$  and  $12 \mu\text{m}$ .

the LWIR region, as shown by an optical image in Fig. 5(a). An infrared image of the case captured by an infrared camera (operating in the wavelength range from 7.5  $\mu\text{m}$  to 14  $\mu\text{m}$ ) at room temperature is shown in Fig. 5(b). As can be observed, the AP and APS samples can be clearly distinguished from the background, since their thermal radiation properties contrast sharply with that of the palm; while, the APSA emitter almost completely blends into the background and becomes invisible to the infrared camera, because its high thermal radiation characteristic matches very closely with the background. In the second case, such samples were put on a carbon nanotube sheet (it is super black over ultra-broadband wavelength range from 300 nm to 20  $\mu\text{m}$ ,) that was mounted on a heating stage and set the temperature as 48  $^{\circ}\text{C}$  [52]. The optical and infrared images of this experimental scenario are presented in Fig. 5(c, d), respectively. It notes that one can still easily see the AP and APS, but it is more difficult to distinguish the APSA from the background in the infrared image. These experiments confirm the practicability of our proposed emitter for thermal infrared camouflage under high thermal radiation background.

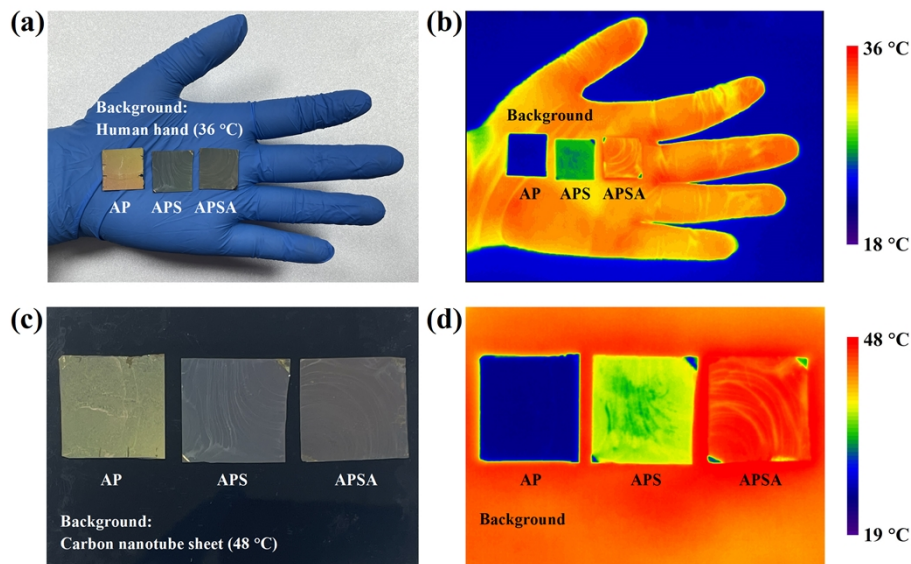


**Fig. 5.** (a) Optical and (b) infrared images of the fabricated AP, APS and APSA samples placed on the author's palm. (c) Optical and (d) infrared images of the fabricated AP, APS and APSA samples placed on a carbon nanotube sheet that was mounted on a heating stage and the temperature set as 48  $^{\circ}\text{C}$ .

Finally, the angular dependence of optical properties of the proposed selective emitter was investigated. Figure 6(a-c) shows the experimental emissivity as a function of wavelength and incident angle for *s*-, *p*- and *un*-polarized light, respectively. Good angle-robust emission performances are observed for all polarizations. The corresponding calculated spectra are presented in Fig. 6(d-f), which are consistent with the experimental results. The origin of the angle-independent emission property is that the APSA structure has a deep-subwavelength thickness (only 1.45  $\mu\text{m}$ ). Figure 6(g) displays the infrared images of the first experimental scenario described above taken at different observation angles, which show that even at large oblique observation angle 60 $^{\circ}$ , favorable camouflage effect of our selective emitter is maintained (see more details in Fig. 10). This feature would bring our emitter beneficial for modern military application in evading large angle detection.

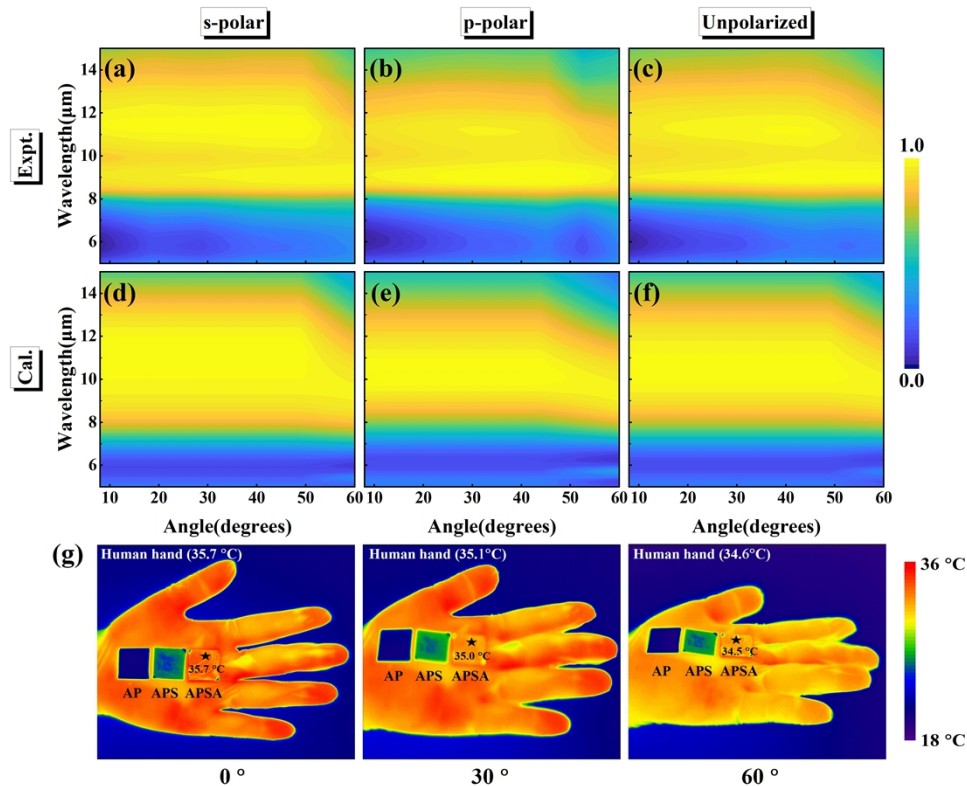


**Fig. 6.** (a-c) Experimental measured and (d-f) calculated emissivity spectra as a function of wavelengths and incident angles for s-, p-, and un-polarized light, respectively. (g) Infrared images of the fabricated AP, APS and APSA samples placed on the author's palm captured at different observation angles (0°, 30°, 60°).

### 3. Conclusion

In conclusion, we have proposed and demonstrated a lithography-free, ultra-thin, high performance LWIR selective emitter for thermal infrared camouflage at high radiation environment. The proposed selective emitter exhibits average emissivity higher than 90% over the range of LWIR atmospheric transparent window from 8-14 μm and low emissivity less than 35% in 5-8 μm non-atmospheric window. Experiment results demonstrate that the selective emitter can really be hidden in high radiation backgrounds. Furthermore, angular dependence of the proposed selective emitter was investigated, the result shows that even at large oblique observation angle 60°, favorable camouflage effect of our selective emitter is maintained. We anticipate that our proposed selective emitter offers great potential for infrared camouflage application in evading large angle detection.

### 4. Experimental section

**Preparation of Ordered Polystyrene Spheres Array:** A 4-inch silicon wafer was firstly hydrophilic treated in a piranha solution (volume ratio of concentrated sulfuric acid and hydrogen peroxide is about 7:3), and then soaked in sodium dodecyl sulfate (SDS) solution (weight ratio



of SDS and water is 10 wt%) for about 48 h to obtain a clean hydrophilic surface. The PS microspheres used in our experiment were purchased from Thermo Fisher Scientific Inc, the size of PS microspheres was 1.8  $\mu\text{m}$  in diameter (2.5 wt%, 15 mL). The PS microspheres aqueous solution was diluted with anhydrous ethanol in a ratio of 1.1:1, and then the solution was ultrasonic for 10 min in an ultrasonic washer until the mixture was uniform. 210  $\mu\text{L}$  PS suspended droplets were pipetted on the pretreated silicon wafer, which would disperse on the silicon wafer to form evenly dispersed PS film. After drying in a closed environment at room temperature, the silicon wafer was slowly immersed in deionized water and formed a self-assembled hexagonal close packed PS monolayer after the water surface stabilized. The prepared substrate was then dipped into the water sink and carefully pulled from the surface of the floating PS film to dry naturally. Thus, the as-prepared PS monolayer can be transferred to the target substrate.

**Device Fabrication:** In the first step, 100 nm Au film was deposited by electron beam evaporation (Syskey Technology) on a cleaned substrate at rate of  $\sim 2 \text{ \AA/s}$ . The substrate was a 20 mm $\times$ 20 mm silicon wafer, which was used to transfer the PS monolayer. This is followed by dipping the substrate into the water sink to transfer the ordered hexagonal PS monolayer to the Au substrate (as presented above). Next step, oxygen plasma reactive ion etching (RIE) was used to reduce the diameter of PS microspheres to obtain the appropriate template size. The etching process was carried out at a radio frequency power of 100 W for 600 seconds. Then, the PS-microsphere-coated Au substrate was heated at 210  $^{\circ}\text{C}$  for 15 min by rapid thermal processing furnace (RTP500V-mini, Beijing East Star) to form a PS hemispherical array under the action of surface tension. The fourth step is to deposit amorphous Si (500 nm) on top of the PS hemispheres at rate of  $\sim 3 \text{ \AA/s}$  using electron beam evaporation. Finally, 7 nm of Au film was deposited on the top at rate of  $\sim 0.5 \text{ \AA/s}$  to form the final selective emitter device.

**Characterization and measurements:** Scanning electron microscope (FEI Sirion 200) with accelerating voltage of 10 kV was used to characterize the morphologies of the multi-layer hemispherical structure. The experimental reflection and transmission spectra were characterized by an FTIR spectrometer (Nicolet iS50, Thermo Fisher Scientific), which was equipped with a reflection module allowing an angle range of  $8^{\circ}$  to  $85^{\circ}$ . The measured reflectance spectrum is normalized with respect to a silver mirror. According to Kirchhoff's law of thermal radiation, the absorptivity equals to emissivity when reaching thermal equilibrium. Since the thickness of the bottom Au film is much thicker than the penetration depth of long-wave infrared light, the transmittance ( $T$ ) of the structure is zero. Therefore, the emissivity ( $E$ ) can be calculated as  $E = A = 1 - R$ .

**Infrared camera imaging:** LWIR images were captured using an IR camera working in the range of 7.5  $\mu\text{m}$  to 14  $\mu\text{m}$  (Fotric 220, the default emissivity is 0.95). In all the measurements, the room temperature was kept at  $\sim 20^{\circ}\text{C}$  and the relative humidity was kept at  $\sim 45\%$ . For data analysis, the apparent temperature curve of the center and peripheral area of the device in the LWIR images was extracted using the AnalyZIR software package.

**Numerical simulations:** The simulations were performed with finite-difference-time-domain (FDTD) method based on commercial package (FDTD solutions, Lumerical Inc.). The upper surface of Au substrate is set as  $z = 0$ . Electromagnetic field distributions were recorded by field profile monitors. The complex dielectric constants of gold and silicon were respectively obtained from the literature [41,53], and the refractive index of polystyrene was set as 1.59 [54].

## Appendix

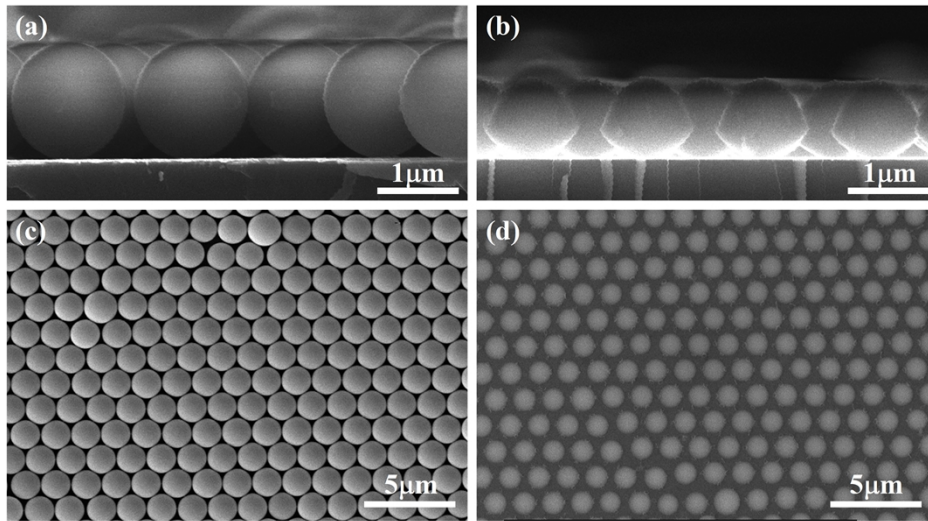


**Fig. 7.** SEM images (Cross-section view and top view) of the experimental sample at two preparation stages: (a, c) Au base-polystyrene microspheres. (b, d) Au base-polystyrene microspheres after oxygen plasma reactive ion etching (RIE).

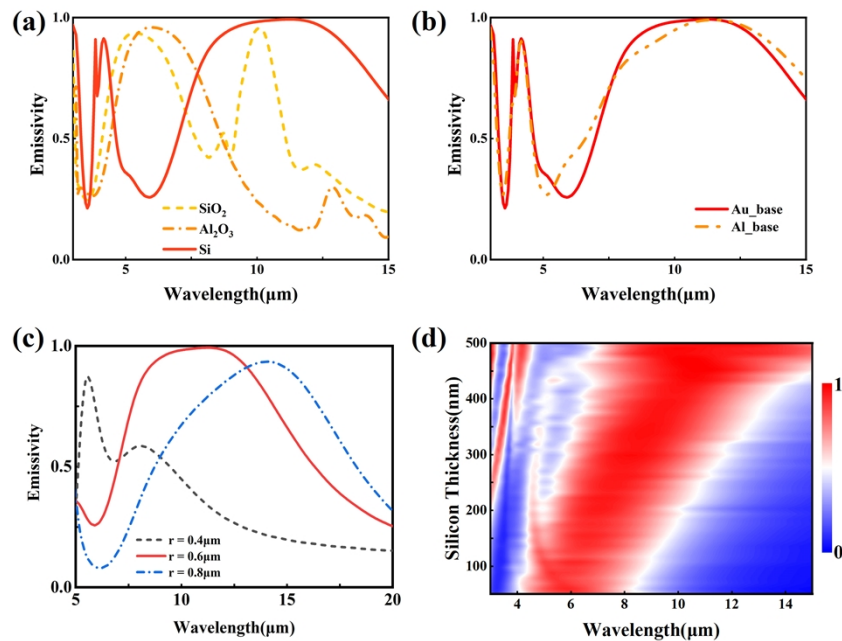


**Fig. 8.** (a) Simulations of emissivity spectra of emitters with different dielectric materials ( $\text{Al}_2\text{O}_3$ ,  $\text{SiO}_2$ , and Si), structure parameters are fixed at  $r = 0.6 \mu\text{m}$ ,  $h = 500 \text{ nm}$  and  $t = 7 \text{ nm}$ . (b) Simulations of emissivity spectra of emitters with different metal substrate (Au and Al), structure parameters are fixed at  $r = 0.6 \mu\text{m}$ ,  $h = 500 \text{ nm}$  and  $t = 7 \text{ nm}$ . (c) Simulations of emission spectra of emitters with different radius of PS hemispheres ( $0.4 \mu\text{m}$ ,  $0.6 \mu\text{m}$  and  $0.8 \mu\text{m}$ ), other structure parameters are fixed at  $h = 500 \text{ nm}$  and  $t = 7 \text{ nm}$ . (d) Simulations of emission spectra of emitters with different thickness of dielectric materials (50 nm-500 nm), other structure parameters are fixed at  $r = 0.6 \mu\text{m}$  and  $t = 7 \text{ nm}$ .

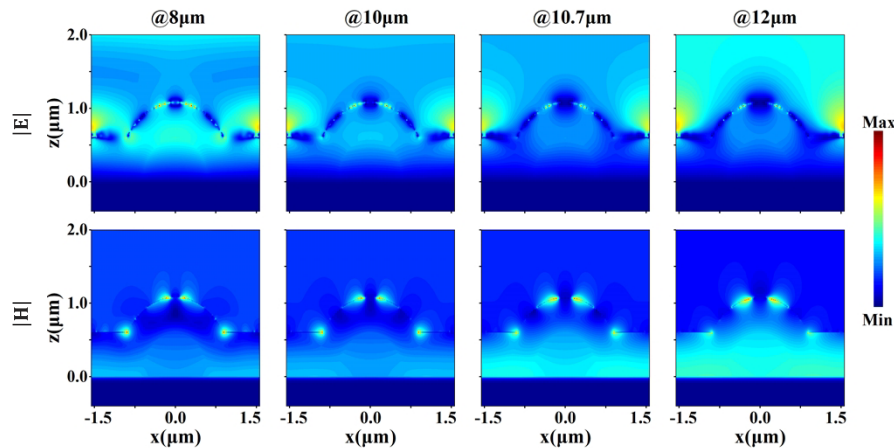


**Fig. 9.** Magnitude of electric fields  $|E|$  and magnetic fields  $|H|$  of the APSA structure in the  $x$ - $z$  plane ( $y = 0$ ) for four different wavelengths 8  $\mu\text{m}$ , 10  $\mu\text{m}$ , 10.7  $\mu\text{m}$  and 12  $\mu\text{m}$ .

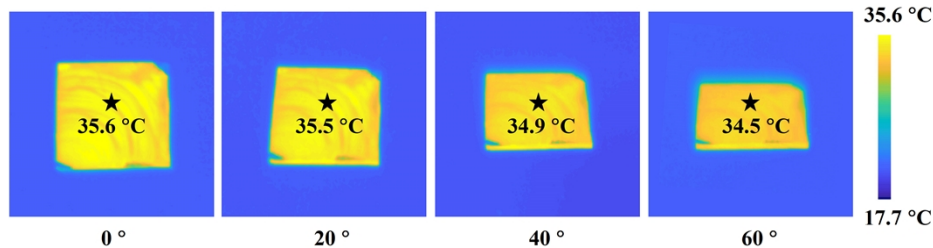


**Fig. 10.** Infrared images of a fabricated APSA absorber sample captured by the LWIR camera (detection wavelength: 8-14  $\mu\text{m}$ ) at different observation angles ranging from  $0^\circ$  to  $60^\circ$ .

**Funding.** National Key Research and Development Program of China (2017YFA0205800); National Natural Science Foundation of China (62075231, 11933006); Science and Technology Commission of Shanghai Municipality (20JC1414603); Shanghai Technology Innovation Project (2021-cyxt1-kj04); China Postdoctoral Science Foundation (2021M703335); Shanghai Municipal Science and Technology Major Project (2019SHZDZX01).

**Disclosures.** The authors declare no conflicts of interest.

**Data availability.** Data underlying the results presented in this paper are not publicly available at this time but may be obtained from the authors upon reasonable request.

## References

1. D. C. Harris, *Materials for Infrared Windows and Domes: Properties and Performance* (SPIE, 1999).
2. S. Fan and W. Li, "Photonics and thermodynamics concepts in radiative cooling," *Nat. Photonics* **16**(3), 182–190 (2022).
3. Z. Chen, L. Zhu, A. Raman, and S. Fan, "Radiative cooling to deep sub-freezing temperatures through a 24-h day-night cycle," *Nat. Commun.* **7**(1), 13729 (2016).
4. A. P. Raman, M. A. Anoma, L. Zhu, E. Rephaeli, and S. Fan, "Passive radiative cooling below ambient air temperature under direct sunlight," *Nature* **515**(7528), 540–544 (2014).
5. X. Pan, H. Xu, Y. Gao, Y. Zhang, L. Sun, D. Li, Z. Wen, S. Li, W. Yu, Z. Huang, J. Wang, B. Zhang, Y. Sun, J. Sun, X. Meng, X. Chen, B. Dagens, J. Hao, Y. Shen, N. Dai, and J. Chu, "Spatial and Frequency Selective Plasmonic Metasurface for Long Wavelength Infrared Spectral Region," *Adv. Opt. Mater.* **6**(20), 1800337 (2018).
6. X. Liu, Z. Li, Z. Wen, M. Wu, J. Lu, X. Chen, X. Zhao, T. Wang, R. Ji, Y. Zhang, L. Sun, B. Zhang, H. Xu, J. Zhou, J. Hao, S. Wang, X. Chen, N. Dai, W. Lu, and X. Shen, "Large-area, lithography-free, narrow-band and highly directional thermal emitter," *Nanoscale* **11**(42), 19742–19750 (2019).
7. W. Jing, S. Zhang, W. Zhang, Z. Chen, C. Zhang, D. Wu, Y. Gao, and H. Zhu, "Scalable and Flexible Electrospun Film for Daytime Subambient Radiative Cooling," *ACS Appl. Mater. Interfaces* **13**(25), 29558–29566 (2021).

8. S. Atigyanun, J. B. Plumley, S. J. Han, K. Hsu, J. Cytrynbaum, T. L. Peng, S. M. Han, and S. E. Han, "Effective Radiative Cooling by Paint-Format Microsphere-Based Photonic Random Media," *ACS Photonics* **5**(4), 1181–1187 (2018).
9. Y. Zhai, Y. Ma, S. N. David, D. Zhao, R. Lou, G. Tan, R. Yang, and X. Yin, "Scalable-manufactured randomized glass-polymer hybrid metamaterial for daytime radiative cooling," *Science* **355**(6329), 1062–1066 (2017).
10. L. Zhang, J. Wang, J. Lou, Y. Zhu, B. Gui, M. Feng, J. Wang, and S. Qu, "A thermally robust and optically transparent infrared selective emitter for compatible camouflage," *J. Mater. Chem. C* **9**(42), 15018–15025 (2021).
11. D. Franklin, S. Modak, A. Vázquez-Guardado, A. Safaei, and D. Chanda, "Covert infrared image encoding through imprinted plasmonic cavities," *Light: Sci. Appl.* **7**(1), 93 (2018).
12. Y. Li, X. Bai, T. Yang, H. Luo, and C. W. Qiu, "Structured thermal surface for radiative camouflage," *Nat. Commun.* **9**(1), 273 (2018).
13. J. Lyu, Z. Liu, X. Wu, G. Li, D. Fang, and X. Zhang, "Nanofibrous Kevlar aerogel films and their phase-change composites for highly efficient infrared stealth," *ACS Nano* **13**(2), 2236–2245 (2019).
14. R. Hu, W. Xi, Y. Liu, K. Tang, J. Song, X. Luo, J. Wu, and C. W. Qiu, "Thermal camouflaging metamaterials," *Mater. Today* **45**, 120–141 (2021).
15. I. Celanovic, N. Jovanovic, and J. Kassakian, "Two-dimensional tungsten photonic crystals as selective thermal emitters," *Appl. Phys. Lett.* **92**(19), 193101 (2008).
16. V. Rinnerbauer, Y. X. Yeng, W. R. Chan, J. J. Senkevich, J. D. Joannopoulos, M. Soljačić, and I. Celanovic, "High-temperature stability and selective thermal emission of polycrystalline tantalum photonic crystals," *Opt. Express* **21**(9), 11482 (2013).
17. T. Kim, J. Y. Bae, N. Lee, and H. H. Cho, "Hierarchical Metamaterials for Multispectral Camouflage of Infrared and Microwaves," *Adv. Funct. Mater.* **29**(10), 1807319 (2019).
18. M. J. Moghimi, G. Lin, and H. Jiang, "Broadband and Ultrathin Infrared Stealth Sheets," *Adv. Eng. Mater.* **20**(11), 1800038 (2018).
19. X. Feng, X. Xie, M. Pu, X. Ma, Y. Guo, X. Li, and X. Luo, "Hierarchical metamaterials for laser-infrared-microwave compatible camouflage," *Opt. Express* **28**(7), 9445 (2020).
20. C. Yang, S. Niu, H. Chang, Y. Wang, Y. Feng, Y. Zhang, G. Li, S. Chen, Y. Qu, and L. Xiao, "Thermal infrared and broadband microwave stealth glass windows based on multi-band optimization," *Opt. Express* **29**(9), 13610 (2021).
21. N. Lee, J. S. Lim, I. Chang, D. Lee, and H. H. Cho, "Flexible Thermocamouflage Materials in Supersonic Flowfields with Selective Energy Dissipation," *ACS Appl. Mater. Interfaces* **13**(36), 43524–43532 (2021).
22. N. Lee, T. Kim, J. S. Lim, I. Chang, and H. H. Cho, "Metamaterial-Selective Emitter for Maximizing Infrared Camouflage Performance with Energy Dissipation," *ACS Appl. Mater. Interfaces* **11**(23), 21250–21257 (2019).
23. J. Kim, C. Park, and J. W. Hahn, "Metal – Semiconductor – Metal Metasurface for Multiband Infrared Stealth Technology Using Camouflage Color Pattern in Visible Range," *Adv. Opt. Mater.* **10**(6), 2101930 (2022).
24. H. B. Shim, K. Han, J. Song, and J. W. Hahn, "A Multispectral Single-Layer Frequency Selective Surface Absorber for Infrared and Millimeter Wave Selective," *Adv. Opt. Mater.* **10**(6), 2102107 (2022).
25. Y. Liu, Z. Feng, C. Xu, A. Chatterjee, and A. A. Gorodetsky, "Reconfigurable Micro- And Nano-Structured Camouflage Surfaces Inspired by Cephalopods," *ACS Nano* **15**(11), 17299–17309 (2021).
26. X. Liu, T. Tyler, T. Starr, A. F. Starr, N. M. Jokerst, and W. J. Padilla, "Taming the blackbody with infrared metamaterials as selective thermal emitters," *Phys. Rev. Lett.* **107**(4), 045901 (2011).
27. M. S. Ergoktas, G. Bakan, E. Kovalska, L. W. Le Fevre, R. P. Fields, P. Steiner, X. Yu, O. Salihoglu, S. Balci, V. I. Fal'ko, K. S. Novoselov, R. A. W. Dryfe, and C. Kocabas, "Multispectral graphene-based electro-optical surfaces with reversible tunability from visible to microwave wavelengths," *Nat. Photonics* **15**(7), 493–498 (2021).
28. D. Lee, S. So, G. Hu, M. Kim, T. Badloe, H. Cho, J. Kim, H. Kim, C.-W. Qiu, and J. Rho, "Hyperbolic metamaterials: fusing artificial structures to natural 2D materials," *eLight* **2**(1), 1 (2022).
29. W. Ma, G. Hu, D. Hu, R. Chen, T. Sun, X. Zhang, Q. Dai, Y. Zeng, A. Alù, C. W. Qiu, and P. Li, "Ghost hyperbolic surface polaritons in bulk anisotropic crystals," *Nature* **596**(7872), 362–366 (2021).
30. Q. Zhang, G. Hu, W. Ma, P. Li, A. Krasnok, R. Hillenbrand, A. Alù, and C. W. Qiu, "Interface nano-optics with van der Waals polaritons," *Nature* **597**(7875), 187–195 (2021).
31. X. Liu, T. Starr, A. F. Starr, and W. J. Padilla, "Infrared spatial and frequency selective metamaterial with near-unity absorbance," *Phys. Rev. Lett.* **104**(20), 207403 (2010).
32. T. Han, X. Bai, D. Gao, J. T. L. Thong, B. Li, and C. W. Qiu, "Experimental demonstration of a bilayer thermal cloak," *Phys. Rev. Lett.* **112**(5), 054302 (2014).
33. L. Phan, W. G. Walkup IV, D. D. Ordinario, E. Karshalev, J. M. Jocson, A. M. Burke, and A. A. Gorodetsky, "Reconfigurable infrared camouflage coatings from a cephalopod protein," *Adv. Mater.* **25**(39), 5621–5625 (2013).
34. H. Zhu, Q. Li, C. Zheng, Y. Hong, Z. Xu, H. Wang, W. Shen, S. Kaur, P. Ghosh, and M. Qiu, "High-temperature infrared camouflage with efficient thermal management," *Light: Sci. Appl.* **9**(1), 60 (2020).
35. M. Pan, Y. Huang, Q. Li, H. Luo, H. Zhu, S. Kaur, and M. Qiu, "Multi-band middle-infrared-compatible camouflage with thermal management via simple photonic structures," *Nano Energy* **69**, 104449 (2020).
36. S. Chandra, D. Franklin, J. Cozart, A. Safaei, and D. Chanda, "Adaptive Multispectral Infrared Camouflage," *ACS Photonics* **5**(11), 4513–4519 (2018).
37. L. Wang, Y. Yang, X. Tang, B. Li, Y. Hu, Y. Zhu, and H. Yang, "Combined multi-band infrared camouflage and thermal management via a simple multilayer structure design," *Opt. Lett.* **46**(20), 5224–5227 (2021).

38. M. Li, D. Liu, H. Cheng, L. Peng, and M. Zu, "Manipulating metals for adaptive thermal camouflage," *Sci. Adv.* **6**(22), eaba3494 (2020).
39. T. Han, X. Bai, J. T. L. Thong, B. Li, and C. W. Qiu, "Full control and manipulation of heat signatures: Cloaking, camouflage and thermal metamaterials," *Adv. Mater.* **26**(11), 1731–1734 (2014).
40. L. Peng, D. Liu, H. Cheng, S. Zhou, and M. Zu, "A Multilayer Film Based Selective Thermal Emitter for Infrared Stealth Technology," *Adv. Opt. Mater.* **6**(23), 1801006 (2018).
41. W. Yu, Y. Lu, X. Chen, H. Xu, J. Shao, X. Chen, Y. Sun, J. Hao, and N. Dai, "Large-Area, Broadband, Wide-Angle Plasmonic Metasurface Absorber for Midwavelength Infrared Atmospheric Transparency Window," *Adv. Opt. Mater.* **7**(20), 1900841 (2019).
42. T. D. Dao, K. Chen, S. Ishii, A. Ohi, T. Nabatame, M. Kitajima, and T. Nagao, "Infrared Perfect Absorbers Fabricated by Colloidal Mask Etching of Al-Al<sub>2</sub>O<sub>3</sub>-Al Trilayers," *ACS Photonics* **2**(7), 964–970 (2015).
43. T. Yokoyama, T. D. Dao, K. Chen, S. Ishii, R. P. Sugavaneshwar, M. Kitajima, and T. Nagao, "Spectrally Selective Mid-Infrared Thermal Emission from Molybdenum Plasmonic Metamaterial Operated up to 1000 °C," *Adv. Opt. Mater.* **4**(12), 1987–1992 (2016).
44. X. Xu, Q. Yang, N. Wattanatorn, C. Zhao, N. Chiang, S. J. Jonas, and P. S. Weiss, "Multiple-Patterning Nanosphere Lithography for Fabricating Periodic Three-Dimensional Hierarchical Nanostructures," *ACS Nano* **11**(10), 10384–10391 (2017).
45. G. Hu, M. Wang, Y. Mazor, C. W. Qiu, and A. Alù, "Tailoring Light with Layered and Moiré Metasurfaces," *Trends Chem.* **3**(5), 342–358 (2021).
46. A. Kohiyama, M. Shimizu, F. Iguchi, and H. Yugami, "Narrowband thermal radiation from closed-end microcavities," *J. Appl. Phys.* **118**(13), 133102 (2015).
47. J. Hao, J. Wang, X. Liu, W. J. Padilla, L. Zhou, and M. Qiu, "High performance optical absorber based on a plasmonic metamaterial," *Appl. Phys. Lett.* **96**(25), 251104 (2010).
48. J. Hao, L. Zhou, and M. Qiu, "Nearly total absorption of light and heat generation by plasmonic metamaterials," *Phys. Rev. B* **83**(16), 165107 (2011).
49. J. Kim, K. Han, and J. W. Hahn, "Selective dual-band metamaterial perfect absorber for infrared stealth technology," *Sci. Rep.* **7**(1), 6740 (2017).
50. J. H. Lee, Y. J. Kim, Y. J. Yoo, S. Chang, G. J. Lee, J. H. Ko, K. M. Kang, D. Chanda, and Y. M. Song, "Colored, Covert Infrared Display through Hybrid Planar-Plasmonic Cavities," *Adv. Opt. Mater.* **9**(17), 2100429 (2021).
51. T. Nobis, E. M. Kaidashev, A. Rahm, M. Lorenz, and M. Grundmann, "Whispering gallery modes in nanosized dielectric resonators with hexagonal cross section," *Phys. Rev. Lett.* **93**(10), 103903 (2004).
52. Y. Jin, T. Zhang, Z. Huang, J. Zhao, Y. Zhao, Z. Wang, L. Lai, J. Wang, K. Jiang, S. Fan, and Q. Li, "Broadband omnidirectional perfect absorber based on carbon nanotube films," *Carbon* **161**, 510–516 (2020).
53. E. D. Palik, *Handbook of Optical Constants of Solids*, 3rd ed. (Academic, 1998).
54. P. Musto, S. Tavone, G. Guerra, and C. De Rosa, "Evaluation by Fourier transform infrared spectroscopy of the different crystalline forms in syndiotactic polystyrene samples," *J. Polym. Sci., Part B: Polym. Phys.* **35**(7), 1055–1066 (1997).